Supplementary Information for "Optimal Trajectories of Brain State Transitions"

Shi Gu[1,2], Richard F. Betzel[2], Marcelo G. Mattar[2], Matthew Cieslak[4], Philip R. Delio[4, 5]
Scott T. Grafton[4], Fabio Pasqualetti[3], Danielle S. Bassett [2, 6]
[1]Applied Mathematics and Computational Science,
University of Pennsylvania, Philadelphia, PA, 19104 USA
[2] Department of Bioengineering,
University of Pennsylvania, Philadelphia, PA, 19104 USA
[3] Department of Mechanical Engineering,
University of California, Riverside, CA, 92521 USA
[4] Department of Psychological and Brain Sciences,
University of California, Santa Barbara, CA, 93106 USA
[5] Neurology Associates of Santa Barbara,
Santa Barbara, CA, 93105 USA
[6] Department of Electrical & Systems Engineering,
University of Pennsylvania, Philadelphia, PA, 19104 USA

December 24, 2016

Contents

List of Figures

List of Tables

1 Supplemental Methods

1.1 Human DSI Data Acquisition and Preprocessing

Both $T1$ weighted anatomical images and diffusion spectrum images (DSI) were acquired from 59 human adults with 72 scans in total, among which 61 scans were acquired from 48 healthy subjects (mean age 22.6 ± 5.1 years, 24 female, 2 left handed) and 11 were acquired from individuals with mild traumatic brain injury [1](mean age 33.8 ± 13.3 years, 4 female, handedness unclear). Participants in the mild traumatic brain injury group were recruited by advertisement and referral from a local neurologist (P.R.D.). Inclusion criteria were age > 18, a history of community acquired concussion in the preceding 10–180 days with persistent cognitive complaints based on self report. Patients with depression were excluded. The concussions were primarily secondary to motor vehicle, bicycle, skateboard and horseback riding accidents. Subjects with an abnormal clinical MRI or CT (eg., skull fracture or hemorrhage) or a preexisting neurologic condition were excluded. All participants volunteered with informed written consent in accordance with the Institutional Review Board/Human Subjects Committee, University of California, Santa Barbara.

DSI scans sampled 257 directions using a $Q5$ half shell acquisition scheme with a maximum b value of 5000 and an isotropic voxel size of 2.4mm. We utilized an axial acquisition with the following parameters: $TR =$ 11.4s, $TE =$ 138ms, 51 slices, FoV (231,231,123 mm). DSI data were reconstructed in DSI Studio (www.dsi-studio.labsolver.org) using q-space diffeomorphic reconstruction (QSDR) [2]. QSDR first reconstructs diffusion weighted images in native space and computes the quantitative anisotropy (QA) in each voxel. These QA values are used to warp the brain to a template QA volume in MNI space using the SPM nonlinear registration algorithm. Once in MNI space, spin density functions were again reconstructed with a mean diffusion distance of 1.25 mm using three fiber orientations per voxel. Fiber tracking was performed in DSI Studio with an angular cutoff of 55°, step size of 1.0 mm, minimum length of 10 mm, spin density function smoothing of 0.0, maximum length of 400 mm and a QA threshold determined by DWI signal in the CSF. Deterministic fiber tracking using a modified FACT algorithm was performed until $100,000$ streamlines were reconstructed for each individual.

1.2 Structural Network Construction

In addition to diffusion scans, a three-dimensional high-resolution T1-weighted sagittal sequence image of the whole brain was obtained at each scanning session by a magnetization-prepared rapid acquisition gradient-echo sequence with the following parameters: TR=15.0ms; TE=4.2ms; flip angle=9 degrees, 3D acquisition, FOV=256mm; slice thickness=0.89mm, matrix=256 ×256. Anatomical scans were segmented using FreeSurfer [3] and parcellated according to the Lausanne 2008 atlas included in the connectome mapping toolkit [4]. A parcellation scheme including 234 regions was registered to the B0 volume from each subject's DSI data. The B0 to MNI voxel mapping produced via QSDR was used to map region labels from native space to MNI coordinates. To extend region labels through the gray/white matter interface, the atlas was dilated by 4mm. Dilation was accomplished by filling non-labeled voxels with the statistical mode of their neighbors' labels. In the event of a tie, one of the modes was arbitrarily selected. Each streamline was labeled according to its terminal region pair.

From these data, we built structural brain networks from each of the 72 diffusion spectrum imaging scans. Consistent with previous work [5, 6, 7, 8, 9, 10, 11, 12, 13], we defined these structural brain networks from the streamlines linking $N = 234$ large-scale cortical and subcortical regions extracted from the Lausanne atlas [4]. We summarize these estimates in a weighted adjacency matrix $\mathbf{A}$ whose entries A_{ij} reflect the structural connectivity between region i and region j (Fig. S1A).

Following [10], here we use an edge weight definition based on the *quantitative anisotropy* (QA). QA is described by Yeh et. al (2010) as a measurement of the signal strength for a specific fiber population $\hat{a}$ in an ODF $\Psi(\hat{a})$ [14, 15]. QA is given by the difference between $\Psi(\hat{a})$ and the isotropic component of the spin density function (SDF, ψ) ISO (ψ) scaled by the SDF's scaling constant. Along-streamline QA was calculated based on the angles actually used when tracking each streamline. Although along-streamline QA is more specific to the anatomical structure being tracked, QA is more sensitive to MRI artifacts such as B1 inhomogeneity. QA is calculated for each streamline. We then averaged values over all streamlines connecting a pair of regions, and used this value to weight the edge between two regions.

1.3 Target Control Model

Here we offer additional derivations related to target control. In particular, we note that if we only care about changing the state of the target regions, then we can modify the control problem discussed in the main text to the following:

$$\begin{aligned} \min_{\mathbf{u}} \quad & \int_0^T (\mathbf{x}_T - \mathbf{x})^T (\mathbf{x}_T - \mathbf{x}) + \rho \mathbf{u}^T \mathbf{u}, \\ s.t. \quad & \dot{\mathbf{x}}(t) = \mathbf{A}\mathbf{x} + \mathbf{B}\mathbf{u}, \\ & \mathbf{x}(0) = \mathbf{x}_0, \\ & \mathbf{x}^{\mathcal{I}}(T) = \mathbf{x}_T^{\mathcal{I}}, \end{aligned} \tag{1}$$

where $\mathcal{I}$ is the index set of the target regions, $\mathcal{I}^c$ the complement, and $\mathbf{x}^{\mathcal{I}}(T)$, $\mathbf{x}_T^{\mathcal{I}}$ are the constraints of the vector to the corresponding regions of $\mathcal{I}$. Similar to the derivation for the optimal control model presented in the main text, we can obtain Eqn[13] and Eqn[14] in the main text but with constraints $\mathbf{p}^{\mathcal{I}^c}(T) = 0$ and $\mathbf{x}^{\mathcal{I}}(T) = \mathbf{x}_T^{\mathcal{I}}$. Without loss of generality, we can assume that $\mathbf{x}(t) = \begin{bmatrix} \mathbf{x}^{\mathcal{I}}(t) \\ \mathbf{x}^{\mathcal{I}^c}(t) \end{bmatrix}$. Otherwise, we can easily reorder the regions before the computations. We then use these constraints in Eqn[16] in the main text, to get

$$\begin{bmatrix} \mathbf{p}^{\mathcal{I}}(T) \\ \mathbf{p}^{\mathcal{I}^c}(T) \end{bmatrix} = \begin{bmatrix} \mathbf{v}_1 \\ \mathbf{v}_2 \end{bmatrix} - \begin{bmatrix} \mathbf{M}_{11} & \mathbf{M}_{12} \\ \mathbf{M}_{21} & \mathbf{M}_{22} \end{bmatrix} \begin{bmatrix} \mathbf{x}^{\mathcal{I}}(T) \\ \mathbf{x}^{\mathcal{I}^c}(T) \end{bmatrix} \tag{2}$$

where $\mathbf{v} = \mathbf{E}_{12}^{-1}(\tilde{\mathbf{c}}_1 - \mathbf{E}_{11}\tilde{\tilde{\mathbf{b}}}_1 - \mathbf{E}_{12}\tilde{\tilde{\mathbf{b}}}_2)$ and $\mathbf{M} = \mathbf{E}_{12}^{-1}\mathbf{E}_{11}$. From Eqn[16], we can get

$$\mathbf{x}^{\mathcal{I}^c}(T) = \mathbf{M}_{22}^{-1}(\mathbf{v}_2 - \mathbf{M}_{21}x^{\mathcal{I}}(T) - \mathbf{p}(T)^{\mathcal{I}^c}) \tag{3}$$

$$\mathbf{p}^{\mathcal{I}}(T) = \mathbf{v}_1 - \mathbf{M}_{11}\mathbf{x}^{\mathcal{I}}(T) - \mathbf{M}_{12}\mathbf{x}^{\mathcal{I}^c}(T) \tag{4}$$

With $\mathbf{p}(T), \mathbf{x}(T)$ on hand, we can follow Eqn[17] in the main text to compute $\tilde{\mathbf{c}}_2$ and then $\tilde{\mathbf{x}}(t)$.

1.4 Specification of the Initial and Target States

In contrast to the model explored in [10], the model we describe above is able to examine *arbitrary* transitions: that is, transitions from any given initial state to any given target state. An important question then is which sets of transitions are biologically relevant for a human brain. As in many complex systems, it is intuitively plausible that not all possible state transitions are required or even healthy [16]. Here, we choose to focus on trajectories whose initial state is the brain's baseline condition: states of high activity in the default mode system, predominantly located in precuneus, posterior cingulate, and superior frontal cortex [17, 18, 19]. We further constrain ourselves to studying the simplest of target states, in which high activity is present in primary sensorimotor cortex: specifically visual, auditory, and motor cortices, which form fundamental drivers for basic human function. Admittedly, many empirically observed brain states are more complex than those we study here, and in fact many activation patterns cannot be clearly partitioned pre-specified cognitive systems. Yet, these simplified settings are reasonable characterizations of a few fundamental activation patterns, and enable us to consider the energetic issues related to the associated control tasks.

1.5 Traditional Notions of Control Strategies

In the main manuscript, we contrast the energy and length of optimal trajectories driven by so-called cognitive control regions of the human brain (located in fronto-parietal, cingulo-opercular, and attention systems) with those driven by regions of the brain theoretically predicted to be effective at 3 unique control strategies studied in the network control literature [10]: *average controllability*, *modal controllability*, and *boundary controllability*. Here we describe these control notions mathematically.

Average Controllability Average controllability of a network equals the average input energy from a set of control nodes and over all possible target states [20]. As a known result, average input energy is proportional to $\text{Trace}(W_K^{-1})$, the trace of the inverse of the controllability Grammian. Instead, we adopt $\text{Trace}(W_K)$ as a measure of average controllability for two main reasons: first, $\text{Trace}(W_K^{-1})$ and $\text{Trace}(W_K)$ satisfy a relation of inverse

proportionality (see Supplementary Methods), so that the information obtained from the two metrics are correlated with one another and, second, W_K is typically very ill-conditioned (see paragraph "Global Controllability") even for coarse network resolutions, so that Trace(W_K^{-1}) cannot be accurately computed even for small brain networks. It should be noted that Trace(W_K) encodes a well-defined control metric, namely the energy of the network impulse response or, equivalently, the network H_2 norm [21]. Regions with high average controllability are, on average, most influential in the control of network dynamics over all different target states.

Modal Controllability Modal controllability refers to the ability of a node to control each evolutionary mode of a dynamical network [22], and can be used to identify states that are difficult to control from a set of control nodes [10]. Modal controllability is computed from the eigenvector matrix $V = [v_{ij}]$ of the network adjacency matrix $\mathbf{A}$. By extension from the PBH test [21], if the entry v_{ij} is small, then the j-th mode is poorly controllable from node i. Following [23], we define $\phi_i = \sum_{j=1}^{N}(1 - \lambda_j^2(A))v_{ij}^2$ as a scaled measure of the controllability of all N modes $\lambda_1(A), \ldots, \lambda_N(A)$ from the brain region i. Regions with high modal controllability are able to control all the dynamic modes of the network, and hence to drive the dynamics towards hard-to-reach configurations.

Boundary Controllability Boundary controllability measures the ability of a set of control nodes to decouple the trajectories of disjoint brain regions [10]. To evaluate the boundary controllability of different brain regions, we proceed as follows. First, we compute a *robust partition* of the brain network as described in [24], and we identify the set of N_1 boundary nodes. We assign to these boundary nodes the boundary controllability value of 1. Second, following [23], we determine the two-partition of the least controllable subnetwork from its Fiedler eigenvector, and we identify the additional boundary nodes. We assign to these boundary nodes the boundary controllability value of $(N - N_1)/N$. Finally, we iterate this process until all nodes have been assigned a boundary controllability value.

1.6 Resting State Data Acquisition and Preprocessing

While in the main manuscript, we study transitions from a binary initial state (DMN regions "on") for simplicity, it is straightforward to generalize the approach to examine fully weighted states. In doing so, the open question is whether the intuitions gained in the binary state case still hold in the weighted state case. We address this question by defining a weighted version of the initial state (DMN) estimated from non-invasive neuroimaging data. Specifically, to extract a continuously-defined default mode state, we examined an independently-acquired resting-state fMRI dataset consisting of 20 individuals each scanned four separate times [25].

Twenty human participants (nine female; ages 19–53 years; mean age = 26.7 years) with normal or corrected vision and no history of neurological disease or psychiatric disorders were recruited for this experiment. All participants volunteered and provided informed consent in writing in accordance with the guidelines of the Institutional Review Board of the University of Pennsylvania (IRB #801929). Participants had no prior experience with the stimuli or the behavioral paradigm. After cleaning to maximize data quality on multiple criteria including subject motion (see [25]), we retained 16 participants (eight female; ages 19-31 years; mean age = 24.1 years), in accordance with accepted good practices in this field [26].

Magnetic resonance images were obtained at the Hospital of the University of Pennsylvania using a 3.0 T Siemens Trio MRI scanner equipped with a 32-channel head coil. T1-weighted structural images of the whole brain were acquired on the first scan session using a three-dimensional magnetization-prepared rapid acquisition gradient echo pulse sequence (repetition time (TR) 1620 ms; echo time (TE) 3.09 ms; inversion time 950 ms; voxel size 1 mm $\times$ 1 mm $\times$ 1 mm; matrix size 190 $\times$ 263 $\times$ 165). A field map was also acquired at each scan session (TR 1200 ms; TE1 4.06 ms; TE2 6.52 ms; flip angle 60 degrees; voxel size 3.4 mm $\times$ 3.4 mm $\times$ 4.0 mm; field of view 220 mm; matrix size 64 $\times$ 64 $\times$ 52) to correct geometric distortion caused by magnetic field inhomogeneity. In all resting state runs, T2*-weighted images sensitive to blood oxygenation level-dependent contrasts were acquired using a slice accelerated multiband echo planar pulse sequence (TR 500 ms; TE 30 ms; flip angle 30 degrees; voxel size 3.0 mm $\times$ 3.0 mm $\times$ 3.0 mm; field of view 192 mm; matrix size 64 $\times$ 64 $\times$ 48).

Cortical reconstruction and volumetric segmentation of the structural data was performed with the Freesurfer image analysis suite [3]. Boundary-Based Registration between structural and mean functional image was performed with Freesurfer *bbregister* [27]. Preprocessing of the resting state fMRI data was carried out using FEAT (FMRI Expert Analysis Tool) Version 6.00, part of FSL (FMRIB's Software Library). The following pre-statistics processing was applied: EPI distortion correction using FUGUE [28]; motion correction using MCFLIRT [29]; slice-timing correction using Fourier-space time series phase-shifting; non-brain removal using BET [30]; grand-

mean intensity normalization of the entire 4D dataset by a single multiplicative factor; highpass temporal filtering (Gaussian-weighted least-squares straight line fitting, with sigma=50.0s). Nuisance time series were voxelwise regressed from the preprocessed data. Nuisance regressors included (i) three translation (X, Y, Z) and three rotation $(pitch, yaw, roll)$ time series derived by retrospective head motion correction ($R = [X, Y, Z, pitch, yaw, roll]$), together with expansion terms ($[R,R^2,R_{t-1},R^2_{t-1}]$), for a total of 24 motion regressors [31]); (ii) the five first principal components of non-neural sources of noise, estimated by averaging signals within white matter and cerebrospinal fluid masks, obtained with Freesurfer segmentation tools and removed using the anatomical CompCor method (aCompCor) [32]; and (iii) an estimate of a local source of noise, estimated by averaging signals derived from the white matter region located within a 15 mm radius from each voxel, using the ANATICOR method [33]. Global signal was also regressed out of the voxel time series due to its demonstrated utility in motion artifact correction [34].

Previous work has demonstrated that the brain's resting activity delineates a task-negative network that overlaps closely with putative default mode network regions [35, 36]. We used a two-stage clustering approach to obtain an estimate of this state. First, we performed clustering at a subject- and scan-specific level. This process entailed extracting the average fMRI BOLD signal (global signal regressed) for each of the 234 brain regions described in the main text, standardizing (z-scoring) regional time series within each session, and clustering brain activity pattern at each time point to one of two clusters based on their similarity (hierarchical agglomerative clustering with distance metric of "correlation" and "average" linkage function). We then obtained cluster centroids by averaging the activity patterns of all time points assigned to either cluster. This resulted in two "states" (clusters) for each individual and for each scan session. Secondly, we performed a group-level clustering analysis. We aggregated cluster centroids across individuals/scan sessions and repeated the same clustering algorithm described earlier. This resulted in a group-level bi-partition of brain activity patterns into two distinct states. Based on a visual inspection and previous descriptions of the default mode network, we considered the first state to be a reasonable estimate of the putative task-negative network. This state exhibited increased activity in frontal, lateral parietal, and temporal cortices along with precuneus, agreeing closely with previous descriptions of the default mode network's topographic distribution [37]. In the Supplemental Results, we use of this continuously-weighted (rather than binary) DMN state to recalculate optimal trajectories to target states.

2 Supplemental Results

2.1 Effect of ρ and Model Reduction

The trajectory of a given task is a curve from the initial state to the target state. When the system is fully controlled, the distance to the target state decreases monotonically along the trajectory. In the common solution, the distance to the target state may increase for a certain period of time (as shown in Fig. 2 in the main text) before decreasing and eventually reaching zero. In our model, the maximal distance to the target state (also referred to as the *extreme distance*) is affected both by the number of control nodes and by the value of the parameter ρ, which balances the contributions of control energy and trajectory distance in the optimization problem. Intuitively, the larger the set of control regions, the smaller the extreme distance, due to a more optimal distribution of input energy (Fig. S1A in this supplement). The role of ρ is also intuitive: when ρ is small, the optimal trajectory could arrive at the target instantly, requiring a massive amount of energy within a short period of time. Although theoretically possible, in practice these large input energies lead to numerical instabilities in the trajectory (Fig. S1B in this supplement). We observe that the trajectory becomes stable when $\rho > 0.01$. In this study, we set $\rho = 1$ to obtain solutions in the stable regime and also to give equal weight to the distance term and the energy term in the optimization problem.

2.2 Relationship between Control Efficiency and Communicability to the Initial State

In the main manuscript, we observed that control efficiency was positively correlated with the network communicability to the target state. Here we ask whether and how control efficiency is related to the network communicability to the initial state (activation of the default mode). We observe that the control efficiency is consistently negatively correlated with the communicability with the initial state (see Fig. S3; note that the negative correlation in the visual transition is not statistically significant). To gain an intuition for these results, we recall that when

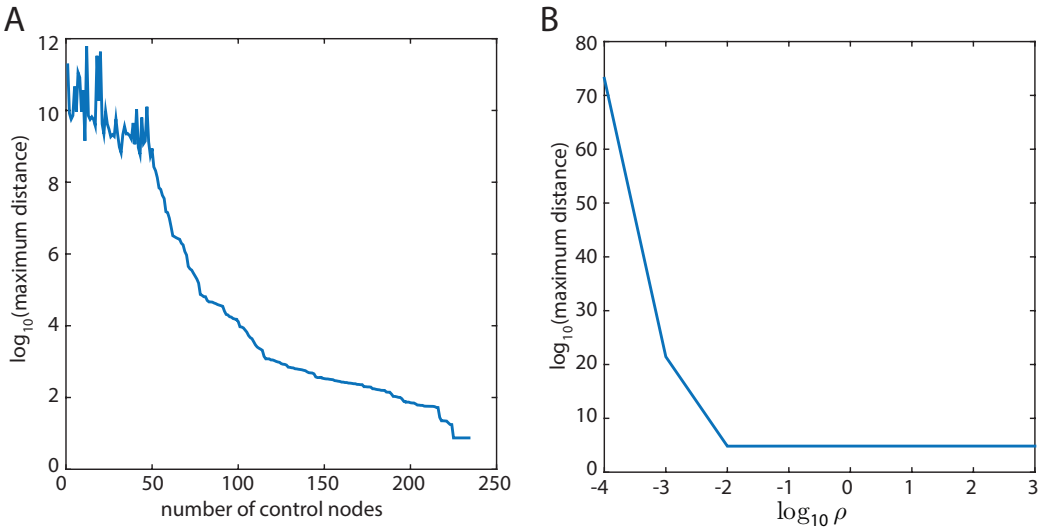

Figure S1: **Numeric Stability of Optimal Trajectories.** Here, we compute the average connectivity matrix across all subjects and we assess the role of the number of control nodes and the value of ρ on the maximal distance to the target state. We note that we observe similar curves across individual subject matrices. *(A)* The trajectory's maximal distance to the target state decreases as the number of control nodes increases. *(B)* The trajectory's maximal distance to the target state decreases as the balance parameter ρ increases. The maximal distance becomes stable when $\rho > 0.01$.

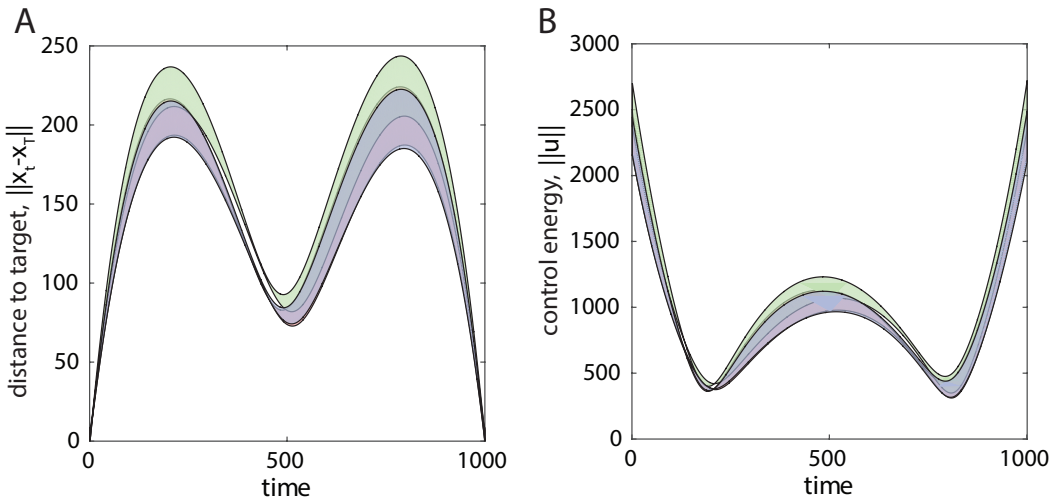

Figure S2: **Distance and Energy of Optimal Trajectories.** *(A)* Envelopes of expected distance to the target state as measured by a standard deviation across subjects. *(B)* Envelopes of the control energy (or input) along the optimal trajectories to the target state, as measured by a standard deviation across subjects. Color indicates the target state: green corresponds to the visual system being the target state, blue corresponds to the auditory system being the target state, and red (in the background) corresponds to the sensorimotor system being the target state.

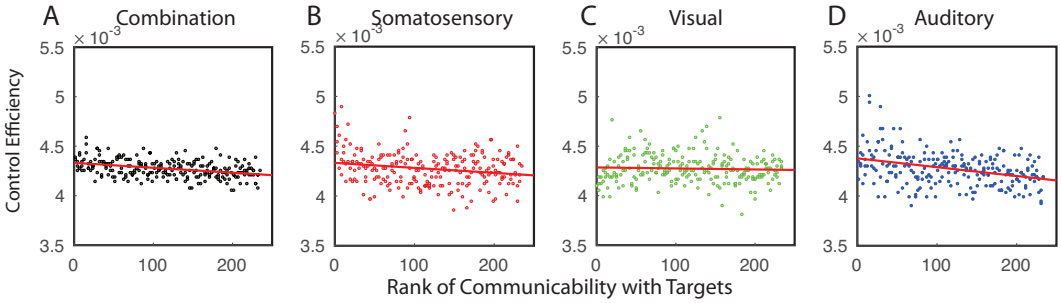

Figure S3: **Correlation between Control Efficiency and the Network Communicability with the Initial State.** Here we show the scatter plot of control efficiency *versus* normalized network communicability with default mode regions: *(A)* overall effect (Spearman $r = -0.33, p = 4.2 \times 10^{-7}$), *(B)* motor ($r = -0.16, p = 1.3 \times 10^{-2}$), *(C)* visual ($r = -0.02, p = 7.8 \times 10^{-1}$) and *(D)* auditory ($r = -0.33, p = 4.2 \times 10^{-7}$).

the brain transitions from the initial state to the target state, the controller needs to increase the activity of the target regions as well as decrease the activity of the initial state. Thus, to be an optimal controller, there exists a *competition* for a region to have high communicability to both the initial state and target states. Our data suggest that the brain displays an interesting assymetry: it produces the most optimal trajectories when control energy is injected into regions with high network communicability to the target state, and low network communicability to the initial state. Note that this assymetry is not required theoretically, and this therefore indicates a potentially important feature of brain structure and dynamics.

2.3 Weighted Initial States: Default Mode Activation Extracted from Resting fMRI

In the main manuscript, we defined the initial state as a binary vector in which the regions of the default mode network had activity magnitudes equal to 1 ("on"), while all other regions had activity magnitudes equal to 0 ("off"). Here we ask whether this specific choice of the initial state affected our results, or whether the same intuitions can be gained using a more continuously weighted notion of the initial state based on DMN activation. To address this question, we estimated the average DMN activation profile from 20 healthy adult human subject undergoing state-of-the-art multiband functional MRI at rest (see Supplemental Methods). We then treated this continuously-valued brain state as the initial state in the estimates of optimal control trajectories. Comparing Figure. S4 in this supplement to Figure. 3 in the main manuscript, we conclude that the use of a continuously-weighted DMN state does not significantly change our results regarding the structurally-driven task preferences of control regions. Indeed, we again find that regions that are close (in terms of walk lengths) to regions of high activity in the target state are efficient controllers for that specific state transition.

Next, comparing Figure. S5 in this supplement to Figure. 4 in the main manuscript, we conclude that the use of a continuously-weighted DMN state does not significantly change our results regarding the regional roles in control tasks. Indeed, we again observe that both the trajectory cost and the energy cost differ by control strategy and by target state. We quantify this observation using a 2-way ANOVA with both the control strategy and target state as categorical factors. Using the trajectory cost as the dependent variable, we observed a significant main effect of control strategy ($F = 77.09, p = 2.38 \times 10^{-40}$), a significant main effect of target state ($F = 30.8, p = 2.83 \times 10^{-13}$), and a significant interaction between control strategy and target state ($F = 10.62, p = 7.6 \times 10^{-12}$). Similarly, using the energy cost as the dependent variable, we observed a significant main effect of control strategy ($F = 64.33, p = 1.05 \times 10^{-34}$), a significant main effect of target state ($F = 38.00, p = 5.45 \times 10^{-16}$), and a significant interaction between control strategy and target state ($F = 9.47, p = 8.13 \times 10^{-10}$).

Finally, comparing Figure. S6 in this supplement to Figure. 5 in the main manuscript, we conclude that the use of a continuously-weighted DMN state does not significantly change our results regarding the specificity of control in health and following injury. Indeed, we again find that the healthy and mTBI group differ in the mean and standard deviation of energetic impact. Specifically, individuals having experienced mTBI displayed significantly lower values of average magnitude of energetic impact (permutation test: $p = 1.0 \times 10^{-5}$) and lower values of the average standard deviation of energetic impact ($p = 2.0 \times 10^{-5}$).

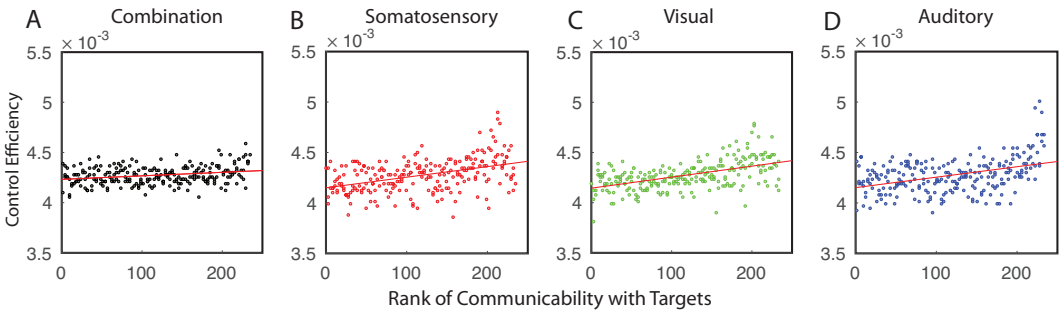

Figure S4: **Structurally-Driven Task Preference for Control Regions.** Using an empirically estimated DMN activation profile as the initial state, we reproduce the analyses reported in main manuscript Figure 3. *(A)* Scatterplot of the control efficiency with the average network communicability to the target regions (Spearman correlation $r = 0.29, p < 4.5 \times 10^{-4}$). *(B–D)* Scatter plot of control efficiency *versus* normalized network communicability with regions that are active in the target state: motor ($r = 0.42$, $p = 2.1 \times 10^{-11}$), extended visual ($r = 0.51$, $p = 1.1 \times 10^{-16}$), and auditory ($r = 0.36$, $p = 1.0 \times 10^{-8}$).

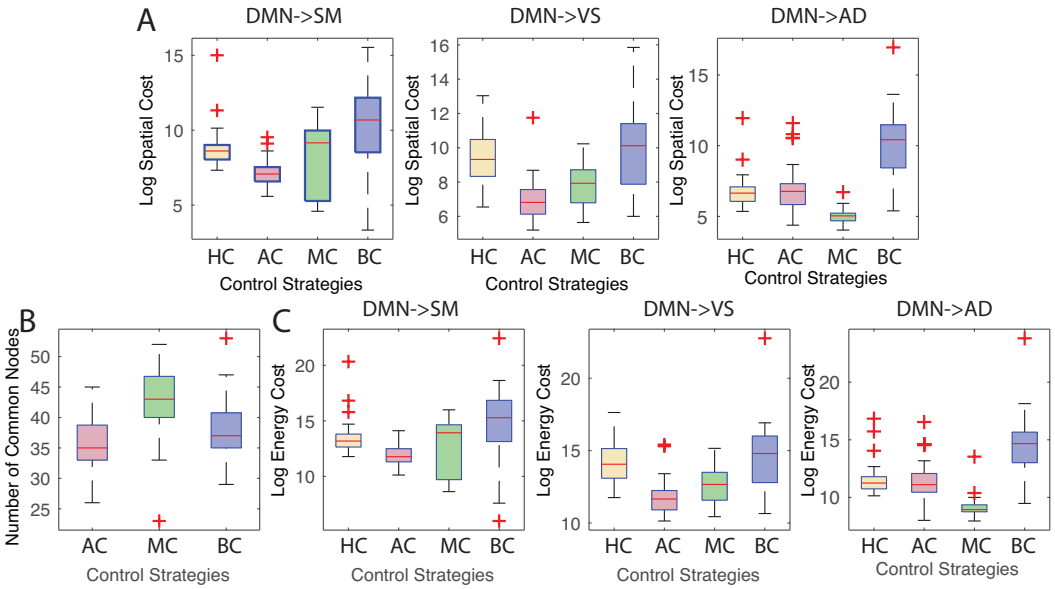

Figure S5: **Regional Roles in Control Tasks.** Using an empirically estimated DMN activation profile as the initial state, we reproduce the analyses reported in main manuscript Figure 4. *(A)* The number of these regions overlapping with the strongest 87 average, modal and boundary control hubs is approximately 40. Different choices of control strategies result in variation in both *(B)* trajectory cost and *(C)* energy cost. Here, HC refers to cognitive control regions, AC refers to average control hubs, MC refers to modal control hubs, and BC refers to boundary control hubs.

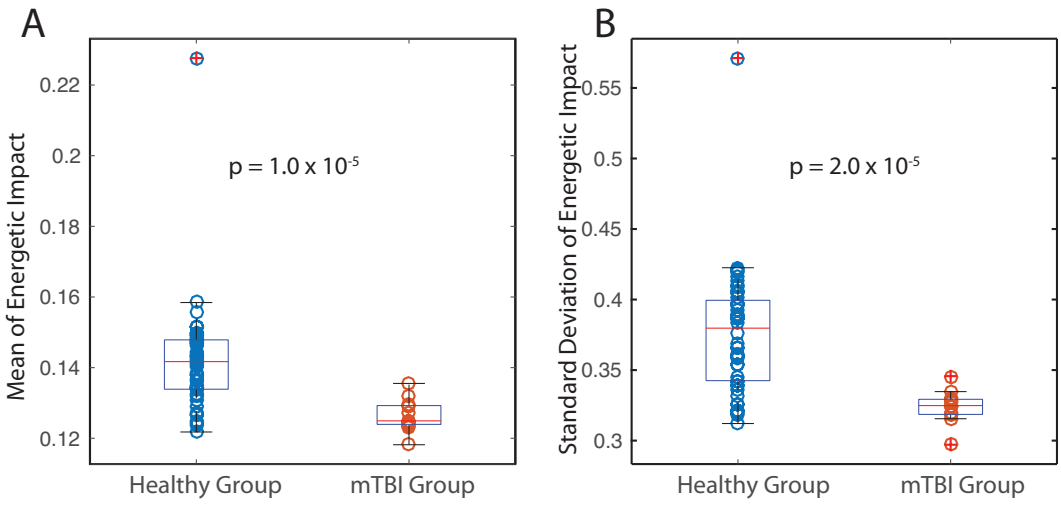

Figure S6: **Specificity of Control in Health and Following Injury.** Using an empirically estimated DMN activation profile as the initial state, we show the magnitude and standard derivation of energetic impact averaged over regions and tasks; boxplots indicate variation over subjects. Even after removing the single outlier in the healthy group, patients with mTBI displayed significantly lower values of average magnitude of energetic impact (permutation test: $p = 1 \times 10^{-5}$) and lower values of the average standard deviation of energetic impact ($p = 2.0 \times 10^{-5}$) than healthy controls.

2.4 Robustness to Perturbation of the Target States

In the main manuscript, we defined the target state as a binary vector in which the regions of (i) auditory, (ii) extended visual or (iii) motor systems had activity magnitudes equal to 1 ("on"), while all other regions had activity magnitudes equal to 0 ("off"). Here we ask whether our results are dependent on this specific choice of the target state. Could the same intuitions could be gained using the target states that were not exactly defined as a "on-off" binary vector? To address this question, we defined the initial state as the same weighted DMN used in Fig. S4 and added identically independent distributed Gaussian noise with $\mu = 0, \sigma = 0.1$ to every region of the target state. Then – following the analyses presented in Figure 3 in the main manuscript – we calculated the control efficiency and plotted it as a function of the network communicability to the target state (see Fig. S7). We observe that regions that are close (in terms of walk lengths) to regions of high activity in the target state are efficient controllers for that specific state transition. These findings indicate that the results reported in the main manuscript are robust to weights on the target states.

3 Control Efficiency and Energetic Impact of Cognitive Control Regions

In the main manuscript, we discuss the control efficiency of randomly selected groups of brain regions in Figure 3. An interesting follow-up question is whether commonly studied cognitive control regions (in dorsal and ventral attention, fronto-parietal and cingulo-opercular areas) have different control efficiency compared to other regions of the brain. To address this question, we compared the control efficiency between cognitive control regions and all other regions of the brain, and we observed no significant differences (Fig. S8; $p > 0.05$ for all comparisons).

In the main manuscript, we also discuss the energetic impact of each brain region. An interesting follow-up question is whether commonly studied cognitive control regions (in dorsal and ventral attention, fronto-parietal and cingulo-opercular areas) have different energetic impact compared to other regions of the brain. To address this question, we compared the energetic impact between cognitive control regions and all other regions of the brain, and we observe that cognitive control areas show lower energetic impact than other brain areas (see Fig. S9). This suggests that the control systems possess more redundancy in their control roles than other regions of the brain.

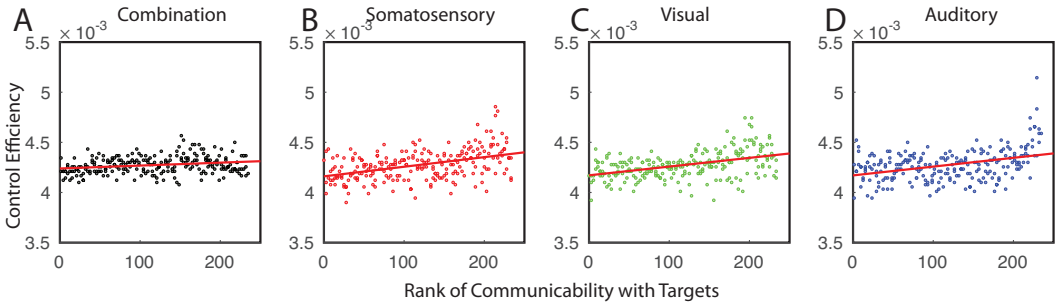

Figure S7: **Structurally-Driven Task Preference for Control Regions.** Using an empirically estimated DMN activation profile as the initial state and using perturbed target states, we reproduce the analyses reported in main manuscript Figure 3. *(A)* Scatterplot of the control efficiency with the average network communicability to the target regions (Spearman correlation $r = 0.22, p < 5.5 \times 10^{-4}$). *(B–D)* Scatter plot of control efficiency *versus* normalized network communicability with regions that are active in the target state: motor ($r = 0.42$, $p = 2.6 \times 10^{-11}$), extended visual ($r = 0.43$, $p = 8.4 \times 10^{-12}$), and auditory ($r = 0.33$, $p = 1.7 \times 10^{-7}$).

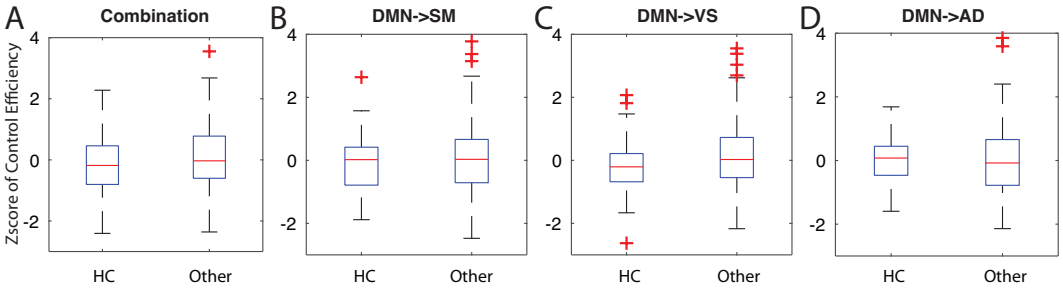

Figure S8: **Regional Preference of Control Efficiency.** We show the control efficiency separately for cognitive control regions (in dorsal and ventral attention, fronto-parietal and cingulo-opercular areas; referred to in the figure as "HC"), and all other regions (referred to in the figure as "Other"), separately for *(A)* all three transitions, *(B)* the transition from the default mode system to the motor system, *(C)* the transition from the default mode system to the extended visual system, and *(D)* the transition from the default mode system to the auditory system. We observe no significant differences between the control efficiency of cognitive control regions and all other regions in the brain.

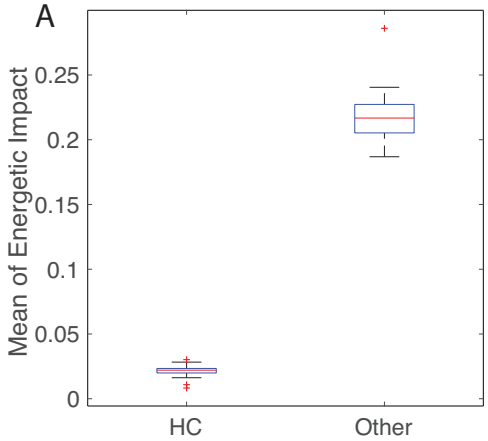

Figure S9: **Regional Preference of Energetic Impact.** Cognitive control regions (in dorsal and ventral attention, fronto-parietal and cingulo-opercular areas; referred to in the figure as "HC") display less energetic impact than other regions (referred to in the figure as "Other") in healthy individuals. Permutation test: $p = 1 \times 10^{-5}$.

3.1 Clinical Sensitivity of Control Statistics vs. Graph Metrics

In the main manuscript, we show that patients with mild Traumatic Brain Injury (mTBI) have significantly lower removal controllability than the healthy group, as measured by lower impact on the required energy for an optimal trajectory following the removal of a node from the control set. Here we ask the question whether this difference between the structural connectomes of the healthy and injured individuals could have been uncovered by arguably simpler and more common graphic metrics. To address this question, we calculated values for seven metrics for each subject, including degree, average shortest path length, clustering coefficient, modularity, global efficiency, and network density (see following section for mathematical definitions). Then, we performed nonparametric permutation tests to determine differences between the healthy and mTBI groups, offering p-values for the hypothesis:

- H_0*: The mTBI and healthy groups displayed the same mean values for a given graph metric;*
- H_1*: The mTBI and healthy groups displayed different mean values for a given graph metric.*

We observed that none of these graphic metrics displayed significant differences between the two groups (see Table. 1 for p-values estimated from non-parametric permutation testing in which the labels of subjects to groups were permuted uniformly at random. These results indicate that the removal controllability offers novel information sensitive to clinical status.

In addition to these graph metrics, we also study whether the mean or variance of the weighted degree is different between the groups. We observe no significant differences (see Fig. S10A–B). we observe no statistically significant differences ($p > 0.05$). We also provide a supplementary figure of the structural connectivity matrices averaged across subject for both groups for comparison (Fig. S10C–D). We observe strong qualitative similarities between the two matrices, consistent with the results of the statistical analyses.

3.2 Regional Roles in Control Tasks for the mTBI Group

In the main manuscript, we show that for healthy subjects, the control efficiency is positively correlated with network communicability. Here we ask the question whether this correlation holds for the patients with mTBI. To address this questions, we calculated the efficiency and communicability on the patients in the mTBI group. Consistent with our observations in the healthy controls, here we observe again that regions that are close (in terms of walk lengths) to regions of high activity in the target state are efficient controllers for that specific state transition (see Fig. S11 and compare to Figure 3 in the main manuscript).

Also in the main manuscript, we show that for healthy subjects, while cognitive control regions cover a broad swath of frontal and parietal cortex, including medial frontal cortex and anterior cingulate (Fig. 4A in the main manuscript), the number of these regions that intersect with the strongest 87 average, modal, or boundary control hubs was less. Interestingly, we find the same phenomenon in the mTBI group (Fig. S12B). These results suggest that cognitive control regions in the human brain may have distinct capabilities necessary for the specific transitions required by the brain under the constraints imposed by neuroanatomy and neurophysiology. Similar to our approach in the healthy group, we more directly tested this possibility by examining the average distance (Fig. S12A) and energy (Fig. S12C) for transitions from the default mode to the auditory, extended visual, and sensorimotor states that are driven by average, modal, and boundary control hubs, or by regions of fronto-parietal, cingulo-opercular, and attention systems. We again observed that both the trajectory cost and the energy cost differ by control strategy and by target state. We quantify this observation using a 2-way ANOVA with both the control strategy and target state as categorical factors. Using the trajectory cost as the dependent variable, we observed a significant main effect of control strategy ($F = 22.58, p = 1.58 \times 10^{-10}$), a significant main effect of target state ($F = 7.82, p = 6.94 \times 10^{-4}$), and a significant interaction between control strategy and target state ($F = 2.85, p = 2.92 \times 10^{-2}$). Similarly, using the energy cost as the dependent variable, we observed a significant main effect of control strategy ($F = 28.04, p = 2.76 \times 10^{-12}$), a significant main effect of target state ($F = 13.0, p = 1.04 \times 10^{-5}$), and a significant interaction between control strategy and target state ($F = 9.47, p = 9.89 \times 10^{-3}$). These results indicate that our main reported results for the healthy control cohort are replicated in the mTBI cohort.

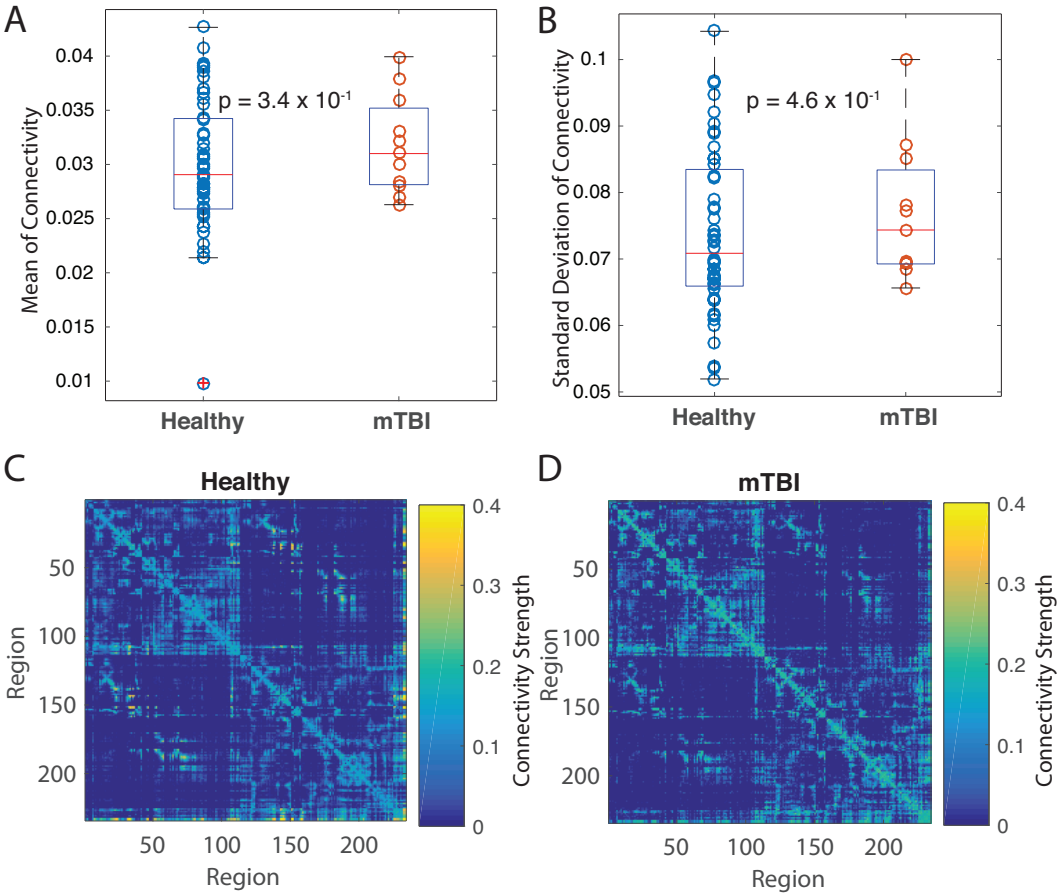

Figure S10: **Difference in Mean and Variance of Connectivity between Healthy and mTBI Cohorts.** Neither *(A)* mean nor *(B)* the standard deviation of edge weights within the structural graphs display any significant difference between the healthy and mTBI groups. Also shown are the structural connectivity matrices averaged across subjects for *(C)* healthy individuals and *(D)* patients who experienced mTBI.

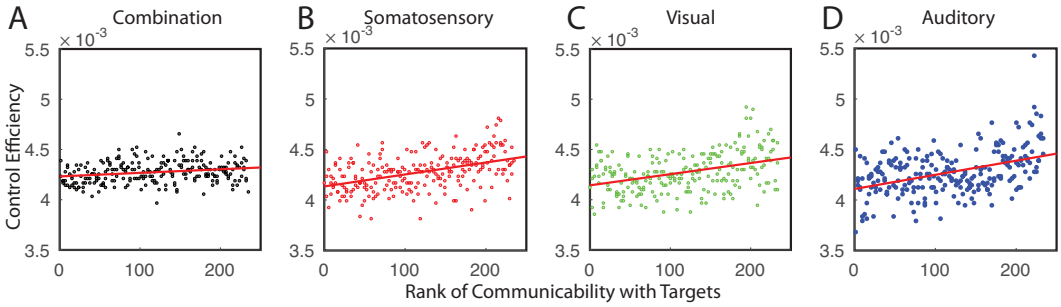

Figure S11: **Correlation between Control Efficiency and Communicability with Targets for Patients with Mild Traumatic Brain Injury.** Here we show the scatter plot of control efficiency *versus* normalized network communicability with regions that are active in target states for patients with mild traumatic brain injury: *(A)* Scatterplot of the control efficiency with the average network communicability to the target regions (Spearman correlation $r = 0.23, p = 3.1 \times 10^{-4}$). *(B–D)* Scatter plot of control efficiency *versus* normalized network communicability with regions that are active in the target state: motor ($r = 0.45, p = 5.3 \times 10^{-13}$), extended visual ($r = 0.36, p = 1.7 \times 10^{-8}$), and auditory ($r = 0.38, p = 2.1 \times 10^{-9}$). Compare to the results reported for the healthy controls in Figure 3 in the main manuscript.

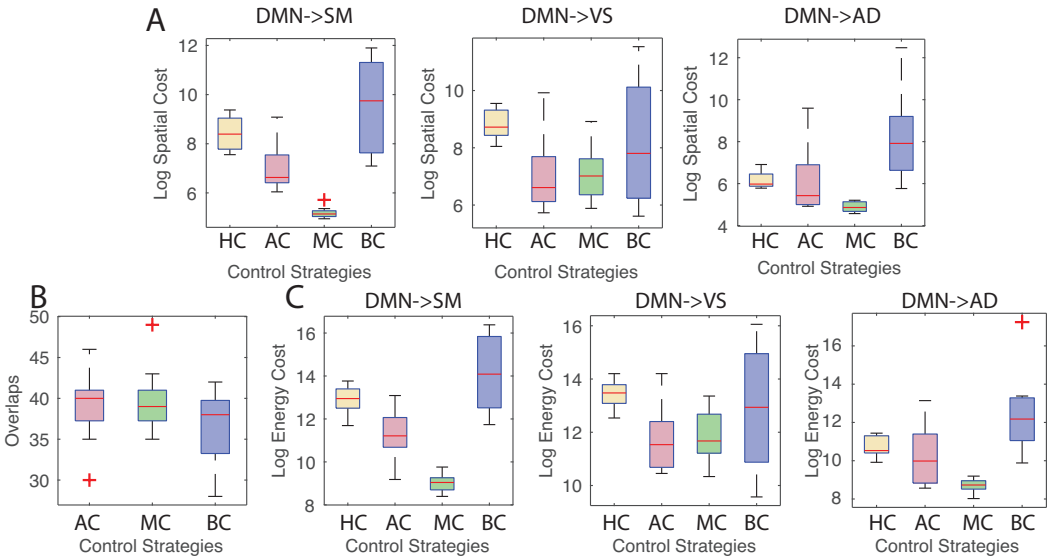

Figure S12: **Regional Roles in Control Tasks for the mTBI group.** Different choices of control strategies result in variation in both *(A)* trajectory cost and *(C)* energy cost. Here, HC refers to cognitive control regions, AC refers to average control hubs, MC refers to modal control hubs, and BC refers to boundary control hubs. Compare to the results reported for the healthy controls in Figure 4 in the main manuscript. *(B)* The number of these regions overlapping with the strongest 87 average, modal and boundary control hubs is approximately 40.

3.3 Specificity of Control in Health and Following Injury: Effect of node elimination on distance cost

In the main manuscript, we observe that both the mean and standard deviation of energetic impact across regions display significant differences between the healthy and mTBI group. Here we ask whether a similar differences could be observed for the distance of the trajectory. We define the trajectory impact in a manner identical to the energetic impact except substituting the trajectory distance for the trajectory energy. Using this approach, we observe that patients with mTBI display a lower trajectory impact than healthy controls (Fig. S13; compare to Figure 5 in the main manuscript). These findings support the notion that mTBI patients display a loss of specificity in putative control roles, suggesting greater susceptibility to damage-induced noise in neurophysiological processes.

3.4 Regional Drivers of Group Differences in Energetic Impact

In the main manuscript, we show that the energetic impact distinguishes the healthy and mTBI group. To further investigate the source of the group difference in energetic impact that we observe at the level of the whole brain, we determine which specific regions displayed the greatest group differences in energetic impact. Using a 2-sample t-test, we observe that the following seven regions showed lower energetic impact in mTBI in comparison to controls ($p < 0.001$, uncorrected): lateral orbitofrontal cortex, 2 subregions within the superior parietal cortex, the banks of the superior temporal sulcus, 2 subregions of the superior temporal cortex, and the putamen. Importantly, two of these areas were located in the attention control circuit, four were located in the target area, and one was located in the subcortex. We next asked whether the weighted degrees of these regions were significantly different between the two groups. We observed that except for one attentional region, the other regions all display significantly lower weighted nodal strength in the healthy group ($p < 0.05$, uncorrected), which is consistent with the relationship between connectivity-to-target and control efficiency (See Figure S4, 7). These results suggest that the changes in control efficiency can be tracked back to alterations of edge weights, but that the sensitivity of metrics to connectome alterations in mTBI is greater for the control efficiency than for the weighted degree.

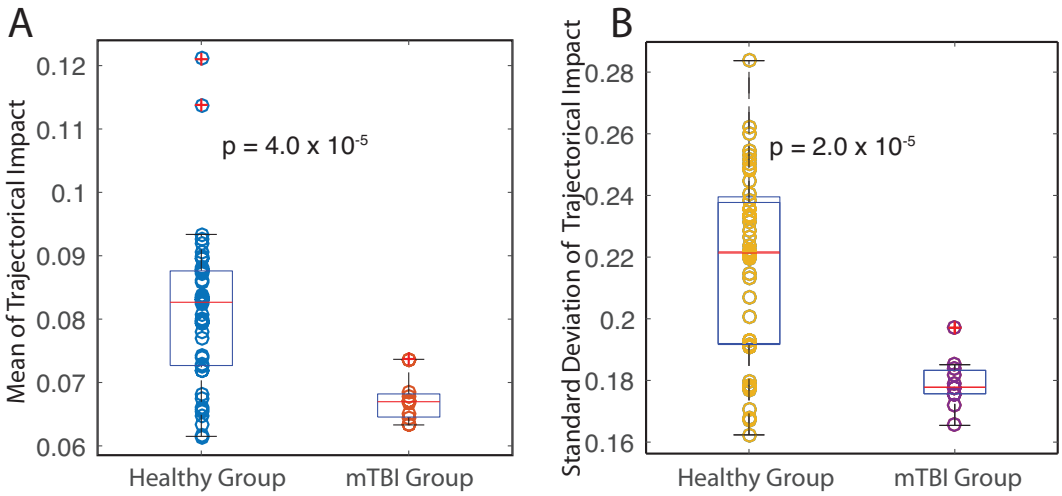

Figure S13: **Specificity of Control in Health and Following Injury: Effect of node elimination on distance cost.** Here we replace the energetic impact with the analogous definition of trajectory impact. As in Figure 5 in the main manuscript, we plot the magnitude and standard derivation of trajectory impact averaged over regions and tasks; boxplots indicate variation over subjects. Patients with mTBI displayed significantly lower values of average magnitude of trajectory impact (permutation test: $p = 4.0 \times 10^{-5}$) and lower values of the average standard deviation of energetic impact ($p = 2.0 \times 10^{-5}$) than healthy controls.

4 Supplemental Discussion

4.1 Energetic versus distance constraints

It is important to mention our considerations in choosing the value of ρ. Note that ρ is the value in the optimization function that tunes the relative contribution of the energetic cost and the trajectory cost. Energetic costs have been frequenctly discussed in the context of brain dynamics across organisms, and indeed are thought to limit both evolution [39] and function [40], driving the costs of establishing and maintaining connections between neural units [41]. These energetic constraints exist at the molecular [42] and tissue [43, 44, 45] scales, and also exist across a wide range of temporal scales [46, 47] impacting on brain state transitions [44, 48, 49, 50]. Distance constraints, on the other hand, effectively tune the smoothness of the trajectory from one state to another, by extension effectively helping to minimize the time of the transition. This constraint is arguably less well-studied, but indicates the intuitive desire to minimize the traversal of brain (and by extension) cognitive states that are not critically necessary for the state transition. This constraint would decrease movement of the brain to states far away from the initial and final states, such as those characteristic of unhealthy cognitive function [51]. Moreover, intuitively the distance constraint could encourage focused transitions [52], rather than transitions that move to many irrelevant states before arriving at the target [53]. Because we are unaware of empirical work offering expicit estimates for the preference of the brain for energetic *versus* distance constraints, we choose the most natural starting point, which is where both constraints provide equal influence on the optimization.

5 Appendix: Mathematical Definitions of Graph Metrics

In this section, we briefly offer mathematical definitions of the several graph metrics that we examined: degree, average shortest path length, clustering coefficient, modularity, global efficiency, and network density.

Degree. The degree k_i of node i is defined as the number of connections emanating from node i: $k_i = \sum_{j \in V} a_{ij}$ where a_{ij} is the adjacency matrix and V is the set of all nodes. Similarly, for a weighted network w_{ij}, we can calculate the weighted degree of i as $k_i^w = \sum_{j \in V} w_{ij}$.

Shortest path length. The shortest path length between node i and node j is defined as the length of the

	DEG	CPL	C-COEF	MODU	L-EFF	G-EFF	DEN
p	0.3635	0.1791	0.4338	0.4208	0.1460	0.3220	0.3635

Table 1: **The p-values for Non-parametric Permutation Tests Assessing Differences in Graphic Metrics Values Between Healthy Adults and Patients with mTBI.** In this table, we list the p-values from the non-parametric permutation tests in which the labels of subjects to groups (healthy or mTBI) are permuted uniformly at random. The p-value is the minimum of the two one-sided p-values with no assumptions on the sign of the difference. Abbreviations are as follows: DEG refers to degree, CPL refers to characteristic path length, C-COEF refers to clustering coefficient, MODU refers to modularity, L-EFF refers to local efficiency, G-EFF refers to global efficiency, and DEN refers to network density.

shortest path starting from node i and ending at node j:

$$d_{ij} = \sum_{a_{uv} \in g_{\{i \leftarrow j\}}} a_{uv}, \tag{5}$$

where $g_{\{i \leftarrow j\}}$ is the shortest path (geodesic) between region i and j. The weighted shortest path length d_{ij}^W between node i and node j is defined using the weighted geodesics as well as the map $w_{ij} \to f(w_{uv})$ from weight to distance.
Characteristic path length. The characteristic path length of the network is defined as average of the shortest paths between all pairs of nodes:

$$L = \frac{1}{n} \sum_{i \in V} L_i, \tag{6}$$

where L_i is the average distance between node i and all other nodes. For weighted graphs, we replace the L_i with the weighted average distance L_i^W.
Clustering coefficient. The clustering coefficient of the network can be defined as the ratio of the number of existing triangles to the number of possible triangles:

$$C = \frac{1}{n} \sum_{i \in V} C_i = \frac{1}{n} \sum_{i \in V} \frac{2t_i}{k_i(k_i - 1)}, \tag{7}$$

where C_i is the clustering coefficient of node i and t_i is the number of triangles attached to node i. For a weighted graph, we can define $C^W = \frac{1}{n} \sum_{i \in V} C_i^W = \frac{1}{n} \sum_{i \in V} \frac{2t_i^W}{k_i(k_i - 1)}$.
Modularity. The modularity of the network is defined as the normalized sum of the modularity function over the given partition:

$$Q = \frac{1}{2m} \sum_{i,j \in V} (a_{ij} - \frac{k_i k_j}{2m}) \delta_{c_i c_j}, \tag{8}$$

where c_i is the cluster label of region i and $2m = \sum_{i,j \in V} a_{ij}$. For a weighted graph, we can define $Q^W = \frac{1}{2m^W} \sum_{i,j \in V} (w_{ij} - \frac{k_i^W k_j^W}{2m^W}) \delta_{c_i c_j}$.
Global efficiency. The global efficiency of a network is defined as the average of the inverse of the shortest path lengths:

$$E = \frac{1}{n} \sum_{i \in V} E_i = \frac{1}{n} \sum_{i \in V} \frac{\sum_{j \in V, j \neq i} d_{ij}^{-1}}{n - 1}, \tag{9}$$

where E_i is the **local efficiency** of node i. For a weighted graph, we can replace the d_{ij} with the weighted distance d_{ij}^W.
Density. The density of the network is defined as the ratio of the number of existing edges to the number of possible edges:

$$d_i = \sum_{ij} \frac{2a_{ij}}{n(n-1)}, \tag{10}$$

where $[a_{ij}]$ is the adjacency matrix and n is the number of nodes.

6 Appendix: Partition of Brain Systems

Here we provide the list of our partition of brain regions in Lausane atlas with 234 regions in Table. 2.

Region	Name	Hemisphere	System
1	lateralorbitofrontal_1	R	ventral_attention
2	lateralorbitofrontal_2	R	ventral_attention
3	lateralorbitofrontal_3	R	ventral_attention
4	lateralorbitofrontal_4	R	ventral_attention
5	parsorbitalis_1	R	cingulo_opercular
6	frontalpole_1	R	fronto_parietal
7	medialorbitofrontal_1	R	fronto_parietal
8	medialorbitofrontal_2	R	fronto_parietal
9	medialorbitofrontal_3	R	fronto_parietal
10	parstriangularis_1	R	fronto_parietal
11	parstriangularis_2	R	fronto_parietal
12	parsopercularis_1	R	cingulo_opercular
13	parsopercularis_2	R	cingulo_opercular
14	rostralmiddlefrontal_1	R	cingulo_opercular
15	rostralmiddlefrontal_2	R	cingulo_opercular
16	rostralmiddlefrontal_3	R	cingulo_opercular
17	rostralmiddlefrontal_4	R	cingulo_opercular
18	rostralmiddlefrontal_5	R	cingulo_opercular
19	rostralmiddlefrontal_6	R	cingulo_opercular
20	superiorfrontal_1	R	default_mode
21	superiorfrontal_2	R	default_mode
22	superiorfrontal_3	R	default_mode
23	superiorfrontal_4	R	default_mode
24	superiorfrontal_5	R	default_mode
25	superiorfrontal_6	R	default_mode
26	superiorfrontal_7	R	default_mode
27	superiorfrontal_8	R	default_mode
28	caudalmiddlefrontal_1	R	fronto_parietal
29	caudalmiddlefrontal_2	R	fronto_parietal
30	caudalmiddlefrontal_3	R	fronto_parietal
31	precentral_1	R	somatosensory
32	precentral_2	R	somatosensory
33	precentral_3	R	somatosensory
34	precentral_4	R	somatosensory
35	precentral_5	R	somatosensory
36	precentral_6	R	somatosensory

37	paracentral_1	R	somatosensory
38	paracentral_2	R	somatosensory
39	paracentral_3	R	somatosensory
40	rostralanteriorcingulate_1	R	cingulo_opercular
41	caudalanteriorcingulate_1	R	cingulo_opercular
42	posteriorcingulate_1	R	default_mode
43	posteriorcingulate_2	R	default_mode
44	isthmuscingulate_1	R	default_mode
45	postcentral_1	R	somatosensory
46	postcentral_2	R	somatosensory
47	postcentral_3	R	somatosensory
48	postcentral_4	R	somatosensory
49	postcentral_5	R	somatosensory
50	supramarginal_1	R	cingulo_opercular
51	supramarginal_2	R	cingulo_opercular
52	supramarginal_3	R	cingulo_opercular
53	supramarginal_4	R	cingulo_opercular
54	superiorparietal_1	R	dorsal_attention
55	superiorparietal_2	R	dorsal_attention
56	superiorparietal_3	R	dorsal_attention
57	superiorparietal_4	R	dorsal_attention
58	superiorparietal_5	R	dorsal_attention
59	superiorparietal_6	R	dorsal_attention
60	superiorparietal_7	R	dorsal_attention
61	inferiorparietal_1	R	fronto_parietal
62	inferiorparietal_2	R	fronto_parietal
63	inferiorparietal_3	R	fronto_parietal
64	inferiorparietal_4	R	fronto_parietal
65	inferiorparietal_5	R	fronto_parietal
66	inferiorparietal_6	R	fronto_parietal
67	precuneus_1	R	default_mode
68	precuneus_2	R	default_mode
69	precuneus_3	R	default_mode
70	precuneus_4	R	default_mode
71	precuneus_5	R	default_mode
72	cuneus_1	R	visual

73	cuneus_2	R	visual
74	pericalcarine_1	R	visual
75	pericalcarine_2	R	visual
76	lateraloccipital_1	R	visual
77	lateraloccipital_2	R	visual
78	lateraloccipital_3	R	visual
79	lateraloccipital_4	R	visual
80	lateraloccipital_5	R	visual
81	lingual_1	R	visual
82	lingual_2	R	visual
83	lingual_3	R	visual
84	fusiform_1	R	visual
85	fusiform_2	R	visual
86	fusiform_3	R	visual
87	fusiform_4	R	visual
88	parahippocampal_1	R	other
89	entorhinal_1	R	visual
90	temporalpole_1	R	other
91	inferiortemporal_1	R	visual
92	inferiortemporal_2	R	visual
93	inferiortemporal_3	R	visual
94	inferiortemporal_4	R	visual
95	middletemporal_1	R	other
96	middletemporal_2	R	other
97	middletemporal_3	R	other
98	middletemporal_4	R	other
99	bankssts_1	R	auditory
100	superiortemporal_1	R	auditory
101	superiortemporal_2	R	auditory
102	superiortemporal_3	R	auditory
103	superiortemporal_4	R	auditory
104	superiortemporal_5	R	auditory
105	transversetemporal_1	R	auditory
106	insula_1	R	fronto_parietal
107	insula_2	R	fronto_parietal
108	insula_3	R	fronto_parietal

109	thalamusproper	R	subcortical
110	caudate	R	subcortical
111	putamen	R	subcortical
112	pallidum	R	subcortical
113	accumbensarea	R	subcortical
114	hyppocampus	R	subcortical
115	amygdala	R	subcortical
116	lateralorbitofrontal_1	L	ventral_attention
117	lateralorbitofrontal_2	L	ventral_attention
118	lateralorbitofrontal_3	L	ventral_attention
119	lateralorbitofrontal_4	L	ventral_attention
120	parsorbitalis_1	L	cingulo_opercular
121	frontalpole_1	L	fronto_parietal
122	medialorbitofrontal_1	L	fronto_parietal
123	medialorbitofrontal_2	L	fronto_parietal
124	parstriangularis_1	L	fronto_parietal
125	parsopercularis_1	L	cingulo_opercular
126	parsopercularis_2	L	cingulo_opercular
127	rostralmiddlefrontal_1	L	cingulo_opercular
128	rostralmiddlefrontal_2	L	cingulo_opercular
129	rostralmiddlefrontal_3	L	cingulo_opercular
130	rostralmiddlefrontal_4	L	cingulo_opercular
131	rostralmiddlefrontal_5	L	cingulo_opercular
132	rostralmiddlefrontal_6	L	cingulo_opercular
133	superiorfrontal_1	L	default_mode
134	superiorfrontal_2	L	default_mode
135	superiorfrontal_3	L	default_mode
136	superiorfrontal_4	L	default_mode
137	superiorfrontal_5	L	default_mode
138	superiorfrontal_6	L	default_mode
139	superiorfrontal_7	L	default_mode
140	superiorfrontal_8	L	default_mode
141	superiorfrontal_9	L	default_mode
142	caudalmiddlefrontal_1	L	fronto_parietal
143	caudalmiddlefrontal_2	L	fronto_parietal
144	caudalmiddlefrontal_3	L	fronto_parietal

145	precentral_1	L	somatosensory
146	precentral_2	L	somatosensory
147	precentral_3	L	somatosensory
148	precentral_4	L	somatosensory
149	precentral_5	L	somatosensory
150	precentral_6	L	somatosensory
151	precentral_7	L	somatosensory
152	precentral_8	L	somatosensory
153	paracentral_1	L	somatosensory
154	paracentral_2	L	somatosensory
155	rostralanteriorcingulate_1	L	cingulo_opercular
156	caudalanteriorcingulate_1	L	cingulo_opercular
157	posteriorcingulate_1	L	default_mode
158	posteriorcingulate_2	L	default_mode
159	isthmuscingulate_1	L	default_mode
160	postcentral_1	L	somatosensory
161	postcentral_2	L	somatosensory
162	postcentral_3	L	somatosensory
163	postcentral_4	L	somatosensory
164	postcentral_5	L	somatosensory
165	postcentral_6	L	somatosensory
166	postcentral_7	L	somatosensory
167	supramarginal_1	L	cingulo_opercular
168	supramarginal_2	L	cingulo_opercular
169	supramarginal_3	L	cingulo_opercular
170	supramarginal_4	L	cingulo_opercular
171	supramarginal_5	L	cingulo_opercular
172	superiorparietal_1	L	dorsal_attention
173	superiorparietal_2	L	dorsal_attention
174	superiorparietal_3	L	dorsal_attention
175	superiorparietal_4	L	dorsal_attention
176	superiorparietal_5	L	dorsal_attention
177	superiorparietal_6	L	dorsal_attention
178	superiorparietal_7	L	dorsal_attention
179	inferiorparietal_1	L	fronto_parietal
180	inferiorparietal_2	L	fronto_parietal

181	inferiorparietal_3	L	fronto_parietal
182	inferiorparietal_4	L	fronto_parietal
183	inferiorparietal_5	L	fronto_parietal
184	precuneus_1	L	default_mode
185	precuneus_2	L	default_mode
186	precuneus_3	L	default_mode
187	precuneus_4	L	default_mode
188	precuneus_5	L	default_mode
189	cuneus_1	L	visual
190	pericalcarine_1	L	visual
191	lateraloccipital_1	L	visual
192	lateraloccipital_2	L	visual
193	lateraloccipital_3	L	visual
194	lateraloccipital_4	L	visual
195	lateraloccipital_5	L	visual
196	lingual_1	L	visual
197	lingual_2	L	visual
198	lingual_3	L	visual
199	lingual_4	L	visual
200	fusiform_1	L	visual
201	fusiform_2	L	visual
202	fusiform_3	L	visual
203	fusiform_4	L	visual
204	parahippocampal_1	L	other
205	entorhinal_1	L	visual
206	temporalpole_1	L	other
207	inferiortemporal_1	L	visual
208	inferiortemporal_2	L	visual
209	inferiortemporal_3	L	visual
210	inferiortemporal_4	L	visual
211	middletemporal_1	L	other
212	middletemporal_2	L	other
213	middletemporal_3	L	other
214	middletemporal_4	L	other
215	bankssts_1	L	auditory
216	bankssts_2	L	auditory

217	superiortemporal_1	L	auditory
218	superiortemporal_2	L	auditory
219	superiortemporal_3	L	auditory
220	superiortemporal_4	L	auditory
221	superiortemporal_5	L	auditory
222	transversetemporal_1	L	auditory
223	insula_1	L	fronto_parietal
224	insula_2	L	fronto_parietal
225	insula_3	L	fronto_parietal
226	insula_4	L	fronto_parietal
227	thalamusproper	L	subcortical
228	caudate	L	subcortical
229	putamen	L	subcortical
230	pallidum	L	subcortical
231	accumbensarea	L	subcortical
232	hyppocampus	L	subcortical
233	amygdala	L	subcortical
234	brainstem	L	other

Table 2: In this table, we list the system allocation of each brain region in Lausane atlas on the scale of 234 regions.

References

[1] M. Cieslak, S. Grafton, Local termination pattern analysis: a tool for comparing white matter morphology, Brain imaging and behavior 8 (2) (2014) 292–299.

[2] F.-C. Yeh, W.-Y. I. Tseng, Ntu-90: a high angular resolution brain atlas constructed by q-space diffeomorphic reconstruction, Neuroimage 58 (1) (2011) 91–99.

[3] A. M. Dale, B. Fischl, M. I. Sereno, Cortical surface-based analysis: I. segmentation and surface reconstruction, Neuroimage 9 (2) (1999) 179–194.

[4] P. Hagmann, L. Cammoun, X. Gigandet, R. Meuli, C. J. Honey, V. J. Wedeen, O. Sporns, Mapping the structural core of human cerebral cortex, PLoS Biol 6 (7) (2008) e159.

[5] D. S. Bassett, D. L. Greenfield, A. Meyer-Lindenberg, D. R. Weinberger, S. W. Moore, E. T. Bullmore, Efficient physical embedding of topologically complex information processing networks in brains and computer circuits, PLoS Comput Biol 6 (4) (2010) e1000748.

[6] D. S. Bassett, J. A. Brown, V. Deshpande, J. M. Carlson, S. T. Grafton, Conserved and variable architecture of human white matter connectivity, Neuroimage 54 (2) (2011) 1262–1279.

[7] A. M. Hermundstad, D. S. Bassett, K. S. Brown, E. M. Aminoff, D. Clewett, S. Freeman, A. Frithsen, A. Johnson, C. M. Tipper, M. B. Miller, et al., Structural foundations of resting-state and task-based functional connectivity in the human brain, Proceedings of the National Academy of Sciences 110 (15) (2013) 6169–6174.

[8] A. M. Hermundstad, K. S. Brown, D. S. Bassett, E. M. Aminoff, A. Frithsen, A. Johnson, C. M. Tipper, M. B. Miller, S. T. Grafton, J. M. Carlson, Structurally-constrained relationships between cognitive states in the human brain, PLoS Comput Biol 10 (5) (2014) e1003591.

[9] F. Klimm, D. S. Bassett, J. M. Carlson, P. J. Mucha, Resolving structural variability in network models and the brain, PLOS Comput Biol 10 (3) (2014) e1003491.

[10] S. Gu, F. Pasqualetti, M. Cieslak, Q. K. Telesford, B. Y. Alfred, A. E. Kahn, J. D. Medaglia, J. M. Vettel, M. B. Miller, S. T. Grafton, et al., Controllability of structural brain networks, Nature communications 6.

[11] S. F. Muldoon, E. W. Bridgeford, D. S. Bassett, Small-world propensity and weighted brain networks, Scientific reports 6.

[12] S. F. Muldoon, F. Pasqualetti, S. Gu, M. Cieslak, S. T. Grafton, J. M. Vettel, D. S. Bassett, Stimulation-based control of dynamic brain networks, arXiv preprint arXiv:1601.00987.

[13] A. Sizemore, C. Giusti, D. Bassett, Classification of weighted networks through mesoscale homological features, arXiv preprint arXiv:1512.06457.

[14] F.-C. Yeh, V. J. Wedeen, W.-Y. I. Tseng, Generalized-sampling imaging, Medical Imaging, IEEE Transactions on 29 (9) (2010) 1626–1635.

[15] D. S. Tuch, Q-ball imaging, Magnetic resonance in medicine 52 (6) (2004) 1358–1372.

[16] S. P. Cornelius, W. L. Kath, A. E. Motter, Realistic control of network dynamics, Nat Commun 4 (2013) 1942.

[17] M. E. Raichle, The brain's default mode network, Annu Rev Neurosci 38 (2015) 433–447.

[18] M. E. Raichle, A. Z. Snyder, A default mode of brain function: a brief history of an evolving idea, Neuroimage 37 (4) (2007) 1083–1090.

[19] M. E. Raichle, A. M. MacLeod, A. Z. Snyder, W. J. Powers, D. A. Gusnard, G. L. Shulman, A default mode of brain function, Proc Natl Acad Sci U S A 98 (2) (2001) 676–682.

[20] B. Marx, D. Koenig, D. Georges, Optimal sensor and actuator location for descriptor systems using generalized Gramians and balanced realizations, in: American Control Conference, Boston, MA, USA, 2004, pp. 2729–2734.

[21] T. Kailath, Linear Systems, Prentice-Hall, 1980.

[22] A. M. A. Hamdan, A. H. Nayfeh, Measures of modal controllability and observability for first-and second-order linear systems, AIAA Journal of Guidance, Control, and Dynamics 12 (3) (1989) 421–428.

[23] F. Pasqualetti, S. Zampieri, F. Bullo, Controllability metrics, limitations and algorithms for complex networks, IEEE Transactions on Control of Network Systems 1 (1) (2014) 40–52.

[24] D. S. Bassett, M. A. Porter, N. F. Wymbs, S. T. Grafton, J. M. Carlson, P. J. Mucha, Robust detection of dynamic community structure in networks, Chaos: An Interdisciplinary Journal of Nonlinear Science 23 (1).

[25] M. G. Mattar, S. L. Thompson-Schill, D. S. Bassett, The network architecture of value learning, arXiv preprint arXiv:1607.04169.

[26] J. E. Desmond, G. H. Glover, Estimating sample size in functional mri (fmri) neuroimaging studies: statistical power analyses, Journal of neuroscience methods 118 (2) (2002) 115–128.

[27] D. N. Greve, B. Fischl, Accurate and robust brain image alignment using boundary-based registration, Neuroimage 48 (1) (2009) 63–72.

[28] M. Jenkinson, Improving the registration of b0-distorted epi images using calculated cost function weights, in: Tenth International Conference on functional mapping of the human brain, 2004.

[29] M. Jenkinson, P. Bannister, M. Brady, S. Smith, Improved optimization for the robust and accurate linear registration and motion correction of brain images, Neuroimage 17 (2) (2002) 825–841.

[30] S. M. Smith, Fast robust automated brain extraction, Human brain mapping 17 (3) (2002) 143–155.

[31] K. J. Friston, S. Williams, R. Howard, R. S. Frackowiak, R. Turner, Movement-related effects in fmri time-series, Magnetic resonance in medicine 35 (3) (1996) 346–355.

[32] Y. Behzadi, K. Restom, J. Liau, T. T. Liu, A component based noise correction method (compcor) for bold and perfusion based fmri, Neuroimage 37 (1) (2007) 90–101.

[33] H. J. Jo, Z. S. Saad, W. K. Simmons, L. A. Milbury, R. W. Cox, Mapping sources of correlation in resting state fmri, with artifact detection and removal, Neuroimage 52 (2) (2010) 571–582.

[34] R. Ciric, D. H. Wolf, J. D. Power, D. R. Roalf, G. Baum, K. Ruparel, R. T. Shinohara, M. A. Elliott, S. B. Eickhoff, C. Davatzikos, R. C. Gur, R. E. Gur, D. S. Bassett, T. D. Satterthwaite, Benchmarking confound regression strategies for the control of motion artifact in studies of functional connectivity, arXiv 1608 03616.

[35] Y. Golland, P. Golland, S. Bentin, R. Malach, Data-driven clustering reveals a fundamental subdivision of the human cortex into two global systems, Neuropsychologia 46 (2) (2008) 540–553.

[36] J. D. Medaglia, T. D. Satterthwaite, T. M. Moore, K. Ruparel, R. C. Gur, R. E. Gur, D. S. Bassett, Flexible traversal through diverse brain states underlies executive function in normative neurodevelopment, arXiv preprint arXiv:1510.08780.

[37] M. D. Greicius, B. Krasnow, A. L. Reiss, V. Menon, Functional connectivity in the resting brain: a network analysis of the default mode hypothesis, Proceedings of the National Academy of Sciences 100 (1) (2003) 253–258.

[38] K. M. Kinnunen, R. Greenwood, J. H. Powell, R. Leech, P. C. Hawkins, V. Bonnelle, M. C. Patel, S. J. Counsell, D. J. Sharp, White matter damage and cognitive impairment after traumatic brain injury, Brain (2010) awq347.

[39] J. E. Niven, S. B. Laughlin, Energy limitation as a selective pressure on the evolution of sensory systems, J Exp Biol 211 (2008) 1792–1804.

[40] D. Attwell, S. B. Laughlin, An energy budget for signalling in the grey matter of the brain, J Cereb Blood Flow and Metab 21 (2001) 1133–1145.

[41] D. S. Bassett, D. Greenfield, A. Meyer-Lindenberg, D. R. Weinberger, S. W. Moore, E. T. Bullmore, Efficient physical embedding of topologically complex information processing networks in brains and computer circuits, PLoS Comput Biol 6 (4) (2010) e1000748.

[42] J. J. Harris, R. Jolivet, E. Engl, D. Attwell, Energy-efficient information transfer by visual pathway synapses, Curr Biol 25 (24) (2015) 3151–3160.

[43] R. C. Sotero, A. Shmuel, Energy-based stochastic control of neural mass models suggests time-varying effective connectivity in the resting state, J Comput Neurosci 32 (3) (2012) 563–576.

[44] J. A. Roberts, K. K. Iyer, S. Vanhatalo, M. Breakspear, Critical role for resource constraints in neural models, Front Syst Neurosci 8 (2014) 154.

[45] A. Tozzi, T. Fla, J. F. Peters, Building a minimum frustration framework for brain functions over long time scales, J Neurosci Res 94 (8) (2016) 702–716.

[46] A. Tozzi, M. Zare, A. A. Benasich, New perspectives on spontaneous brain activity: Dynamic networks and energy matter, Front Hum Neurosci 10 (247).

[47] T. Proix, F. Bartolomei, P. Chauvel, C. Bernard, V. K. Jirsa, Permittivity coupling across brain regions determines seizure recruitment in partial epilepsy, J Neurosci 34 (45) (2014) 15009–15021.

[48] G. Deco, E. T. Rolls, R. Romo, Stochastic dynamics as a principle of brain function, Prog Neurobiol 88 (1) (2009) 1–16.

[49] K. Friston, J. Kilner, L. Harrison, A free energy principle for the brain, Journal of Physiology-Paris 100 (1) (2006) 70–87.

[50] K. Friston, The free-energy principle: a unified brain theory?, Nature Reviews Neuroscience 11 (2) (2010) 127–138.

[51] A. N. Khambhati, K. A. Davis, T. H. Lucas, B. Litt, D. S. Bassett, Virtual cortical resection reveals push-pull network control preceding seizure evolution, Neuron 91 (5) (2016) 1170–1182.

[52] M. D. Fox, A. Z. Snyder, D. M. Barch, D. A. Gusnard, M. E. Raichle, Transient BOLD responses at block transitions, Neuroimage 28 (4) (2005) 956–966.

[53] J. Posner, C. Park, Z. Wang, Connecting the dots: a review of resting connectivity MRI studies in attention-deficit/hyperactivity disorder, Neuropsychol Rev 24 (1) (2014) 3–15.